Electric-field-induced insulator to Coulomb glass transition via oxygen-vacancy migration in Ca-doped $BiFeO_3$

Ji Soo Lim,[1] Jin Hong Lee,[1] Atsushi Ikeda-Ohno,[2] Takuo Ohkochi,[3] Ki-Seok Kim,[4] Jan Seidel,[5] and Chan-Ho Yang[1,6,*]

[1]*Department of Physics, KAIST, Daejeon 34141, Republic of Korea*

[2]*Institute of Resource Ecology, Helmholtz-Zentrum Dresden-Rossendorf (HZDR), Bautzner Landstraße 400, D-01328 Dresden, Germany*

[3]*Japan Synchrotron Radiation Research Institute, SPring-8, Sayo, Hyogo 679–5198, Japan*

[4]*Department of Physics, POSTECH, Pohang, Gyeongbuk 790-784, Republic of Korea*

[5]*School of Materials Science and Engineering, The University of New South Wales, Sydney, New South Wales 2052, Australia*

[6]*Institute for the NanoCentury, KAIST, Daejeon 34141, Republic of Korea*

(Received 28 January 2016; revised manuscript received 27 June 2016; published 11 July 2016)

The multiferroic $BiFeO_3$ (BFO) as a charge-transfer-type insulator is an interesting system in which to explore correlated electronic conduction. Here, we substitute divalent Ca ions into the parent BFO and apply an external electric field at elevated temperatures to spatially redistribute spontaneously created oxygen vacancies, thereby generating hole carriers in regions of less dense oxygen-vacancy concentrations. X-ray diffraction and photoemission spectroscopic measurement are employed to quantify a large variation of local oxygen-vacancy concentration, as much as $\sim 10^{21}$ cm^{-3}, and explore the consequent evolution of electronic band structure. We find that a nonrigid polaronic band is created by hole doping as a result of a strong electron-lattice coupling. We also show strong evidence for the disorder-driven formation of a Coulomb-glass state through electronic transport measurements on a quantitative level. These spectroscopic and transport results can be combined and understood in the framework of intrinsic spatial inhomogeneity of the polaronic charge density. The finding not only offers a promising platform and methodology for examining the interplay of functional defects and correlated electronic behaviors, but also suggests a unique electronic conduction mechanism applicable to systems with coexistence of strong electron correlation, electron-lattice interaction, and randomness beyond the Coulomb-glass physics in semiconductors.

DOI: 10.1103/PhysRevB.94.035123

I. INTRODUCTION

Oxygen vacancies are omnipresent in oxide compounds and can critically influence electronic conduction phenomena in correlated oxides, which manifest themselves, e.g., as metal-insulator transitions, high-T_c superconductivity, magnetoresistance, and resistive switching phenomena [1–4]. Recently, oxygen vacancies have been regarded as an active control parameter to adjust the physical properties and induce emerging states and functionalities [4–11] beyond their traditional role as an intrinsic defect formed according to thermodynamic stability [12]. Since ionized oxygen vacancies are donors to create double electrons, their existence can directly influence electronic conduction by band filling [5,13] and increase the extent of disorder, leading to strong localization [14,15]. In addition, the antiparticle nature of oxygen anions and the relatively high ionic mobility enable the transfer of positive defects in an electric way and the creation of a nonequilibrium state locally [5,6]. Despite the potential usability of oxygen-vacancy control to find new conducting quantum phases, studies so far apparently still remain at the conceptual level, and it is also not entirely satisfactory to quantify local oxygen-vacancy concentrations. Furthermore, it has been challenging to understand delicate features of electronic transport and band structure of local conducting regions on a quantitative level.

In this respect, Ca-doped BFO ($Bi_{1-x}Ca_xFeO_{3-\delta}$; BCFO) is an interesting compound because it contains a large amount of oxygen vacancies ($\delta = x/2$) spontaneously produced to maintain the valence state of Fe^{3+}, and the oxygen-vacancy density in the as-grown state can be controlled by the Ca content (x) [5,10,16–19]. The parent compound is a well-known multiferroic with strong electron correlation and large instabilities both electric and magnetic [20,21], and its electronic conduction at domain walls has attracted particular attention [13,22,23]. In this paper, we show that electrical formation of BCFO at an elevated temperature with large modulation of the oxygen-vacancy concentration can realize a hole-doped system with exotic electronic conduction explained within the context of the Coulomb-glass theory, i.e., the formation of a system with states localized by disorder and long-range interactions between particles [24], in conjunction with the emergence of a nonrigid band associated with strong electron-lattice coupling. We discuss the experimental observations based on polaronic charge inhomogeneity and localization at charge-cloud boundaries, where the emergent band plays an important role. These prominent property changes by electrical control of oxygen vacancies hold promise for additional electronic and optical functionalities.

II. ELECTRICAL FORMATION OF NONEQUILIBRIUM OXYGEN-VACANCY DISTRIBUTION AND QUANTIFICATION OF OXYGEN-VACANCY CONTENT

To create the conducting phase by an external electric field, coplanar platinum electrodes were deposited on top of BCFO films with homogeneously distributed oxygen vacancies in the as-grown state [Fig. 1(a); see Appendixes A and B]. Oxygen vacancies as positively charged ions easily migrate

*Author to whom correspondence should be addressed: chyang@kaist.ac.kr

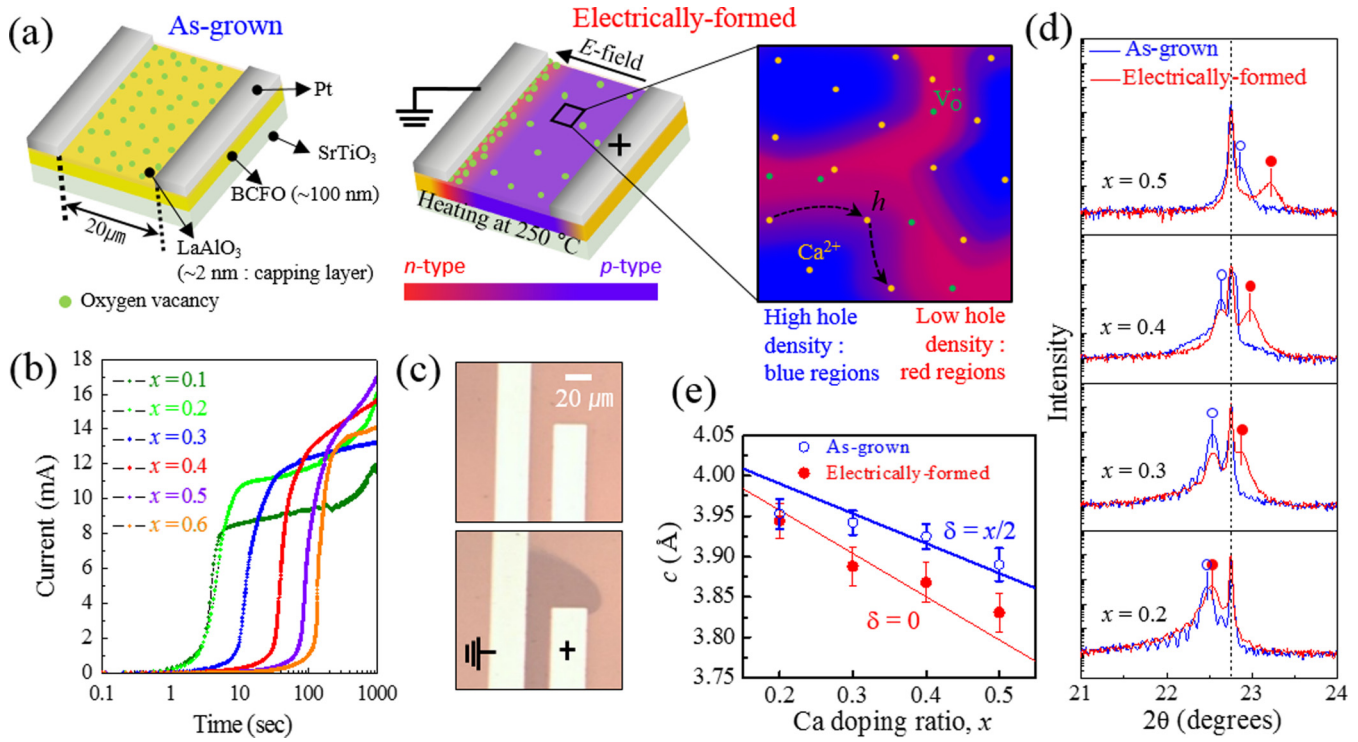

FIG. 1. Electrical formation process for a nonequilibrium oxygen-vacancy distribution in BCFO films. (a) Schematics of a BCFO thin film with a pair of platinum coplanar electrodes for the as-grown insulating state (left) and the electrically formed hole-doped state (middle) where mobile oxygen vacancies are electrically removed. (Right) Proposed microscopic conduction mechanism in the hole-doped state. Phase separation occurs as a result of the strong electron-lattice coupling and the randomness due to dopants. The major electronic conduction at low temperatures is done by hopping of the localized holes along the boundaries between the high- and low-hole-density regions. (b) *In situ* real-time electrical current measurement as a function of elapsed time during an electrical formation process at a bias of 15 V. (c) Microscopic images for an as-grown area (top) and the electrically formed area (bottom). (d) X-ray diffractions for (001) film and substrate peaks. (e) c-axis lattice parameters of BCFO films. The error bar indicates the full width at half maximum of the diffraction peak.

in an external electric field at 250 °C and accumulate near the negatively biased electrode. Most of the interelectrode areas contain few oxygen vacancies in contrast to divalent Ca^{2+} ions which are homogeneously distributed. Accordingly, the electrical formation process yields a hole-doped system because the nonequilibrium distribution of oxygen vacancies is nearly frozen after quenching to room temperature. For a better understanding of the electromigration, we monitored the current between the coplanar electrodes *in situ* during the formation. It was observed that the current value abruptly increased by six orders of magnitude at the moment when a conducting path connected the electrodes [Fig. 1(b)]. Conducting regions nucleate near the positively biased electrode and grow toward the opposite electrode. The current after the steep increase became slowly saturated, commensurate with the expansion of the conducting regions. The higher the Ca substitution ratio, the longer time was taken to establish the first conducting channel because the initial oxygen-vacancy concentration in the as-grown state is proportional to x. Initial insulating states for all x were optically transparent with a yellowish color, but the formed areas exhibited dark contrast [Fig. 1(c)]. This nonequilibrium distribution could be turned back into the original homogeneous distribution by keeping samples at 250 °C for 2 h in atmosphere.

The amount of migrated oxygen vacancies was estimated by measuring the variation of the c-axis lattice parameter using x-ray diffraction because the existence of oxygen vacancies tends to expand the volumes of oxide materials [25,26]. The electrical formation for BCFO also causes significant changes in c-axis lattice parameters [Figs. 1(d) and 1(e)]. To quantify the oxygen-vacancy content based on Vegard's law, we calculated two interpolated lines between the two end compounds, i.e., $x = 0$ and 1, for the as-grown compounds with the fixed valence state of Fe^{3+} ($\delta = x/2$) and the stoichiometric compounds ($\delta = 0$). Oxygen content was determined by comparing the measured c-axis lattice parameter with a linear interpolation value between these two Vegard lines at a given x. Except for $x = 0.2$ near the phase boundary of the doping-driven ferroelectric to nonferroelectric transition [5], the c-axis lattice parameter of all doping ratios approaches the Vegard line at $\delta = 0$ after the electrical formation, indicating that the number of migrated oxygen vacancies is of a similar order of magnitude to that in the as-grown state. We note that this variation of oxygen-vacancy concentration (e.g., $\Delta n_{ov} \sim 2.5 \times 10^{21}$ cm^{-3} for $\Delta\delta \sim 0.15$ at $x \sim 0.3$) is a huge change that can have a large impact on physical properties, taking into account that thermal annealing of bulk samples at $x = 0.3$ in a high-pressure oxygen environment at ~125 bar resulted in an order-of-magnitude smaller variation ($0 < \Delta\delta < 0.016$) [27].

This estimation of oxygen content can be reconfirmed by x-ray photoelectron spectroscopy (XPS) for the oxygen 1s binding energy (Fig. 2). The small peak at 531 eV arises from

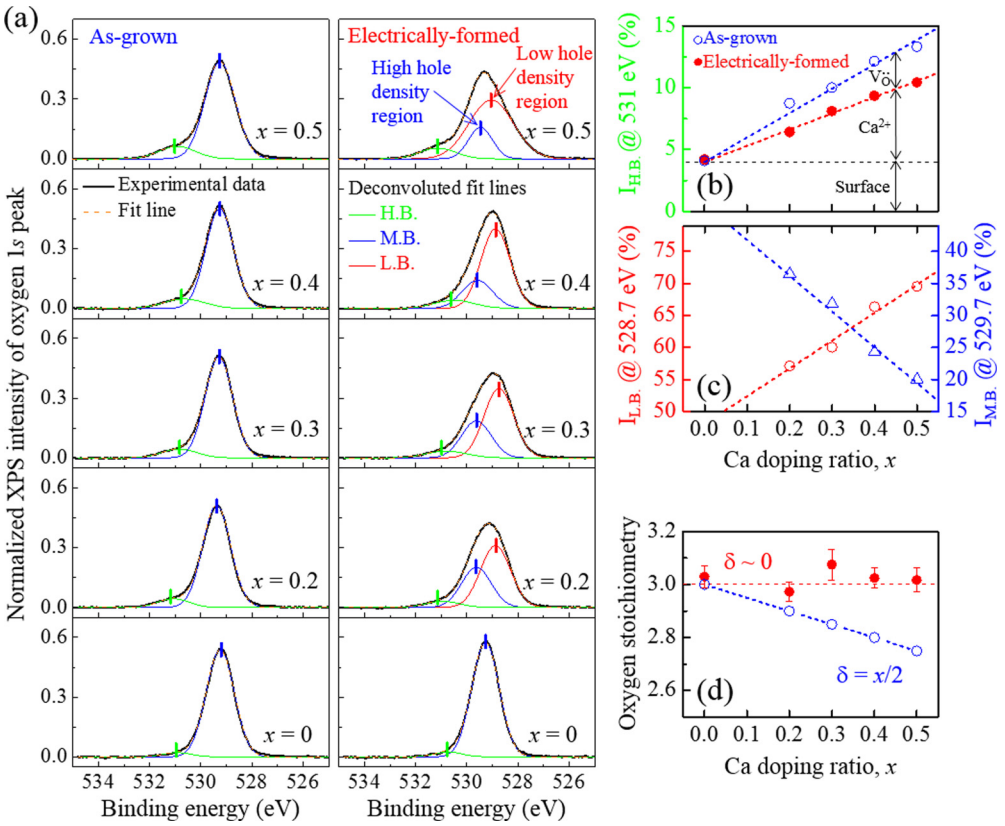

FIG. 2. Estimation of oxygen stoichiometry using XPS. (a) Oxygen 1s XPS spectra measured in the as-grown and electrically formed regions at the selected x. The XPS intensity was normalized by the integrated intensity of the Fe 2p XPS peak. These spectra can be deconvoluted into two or three Gaussian peaks which are named high binding (H.B.), medium binding (M.B.), and low binding (L.B.) peaks, according to the peak position. (b) The areal fraction of the oxygen H.B. peak. (c) The areal fraction of the M.B. and L.B. peaks plotted as functions of x. (d) The total integrated intensity of the oxygen XPS spectrum represents the oxygen content relative to the Fe content. Assuming the Fe^{3+} valence state and charge neutrality in all the as-grown samples, i.e., $Bi_{1-x}Ca_xFeO_{3-\delta}$ ($\delta = x/2$), we can determine the relative oxygen stoichiometry ($3-\delta$) of the electrically formed area to be nearly 3.

intrinsic screening effects of neighboring Ca ions or oxygen vacancies as well as from extrinsic surface contaminations. The extrinsic effect is almost identical for all samples while the portion of Ca ion contribution linearly increases with x. Subtraction of the electrically formed spectrum from the as-grown one gives the oxygen-vacancy contribution. As the total spectral weight of the oxygen 1s peak is proportional to oxygen content, it enables quantification of oxygen stoichiometry as summarized in Fig. 2(d), which is consistent with the above-mentioned result of x-ray diffraction.

In addition, the major single peak on the right-hand side became broader and asymmetric after electrical formation, indicating that the hole-doped samples were spatially inhomogeneous [see the enlarged schematic in Fig. 1(a)], due to formation of polaron clouds [28–31]. It is thought that phase separation occurs on a length scale of less than 100 nm, because the photoemission electron microscopy (PEEM) result (which will be addressed later in this paper) turned out to be uniform at a spatial resolution of ~100 nm. Moreover, the correlation length, which could be estimated by the broadness of the x-ray diffraction peak according to the Scherrer formula [32], decreased from ~100 nm, limited by film thickness, in as-grown films to ~60 nm at $x = 0.3$ and 0.4 by electrical formation.

III. ELECTRONIC CONDUCTION PROPERTY

By virtue of these efforts, we were ready to explore electronic transport properties at a quantitative level. Although resistance was measurable even at low temperatures down to, e.g., 75 K at $x = 0.6$ owing to the drastic increase of conductivity, its temperature dependence turned out to be still semiconducting, indicating an unusual localization mechanism even at such high hole-doping ratios. The logarithmic plot of the measured resistance exhibited a linear dependence of $T^{-1/2}$ at low temperatures [Fig. 3(a)] but it was transformed to the normal semiconducting curve characterized by an increase inversely proportional to temperature at high temperatures [Fig. 3(b)]. The point where the transport behavior starts to deviate from the $T^{-1/2}$ dependence, i.e., the crossover temperature (T_x), is marked by an arrow in the plot. This observation is reminiscent of the disorder-driven Efros-Shklovskii variable-range hopping (ES-VRH) [24]. A similar transport behavior has been observed in doped semiconductors [33,34] and analyzed in the context of the Coulomb glass [24,35,36]. The clearance of oxygen vacancies lowers the chemical potential to a level below the valence band maximum and seems to induce a metallic conduction at high nominal carrier concentrations. However, disorder can localize the band edge and thus thermal excitation from a filled state below the lower

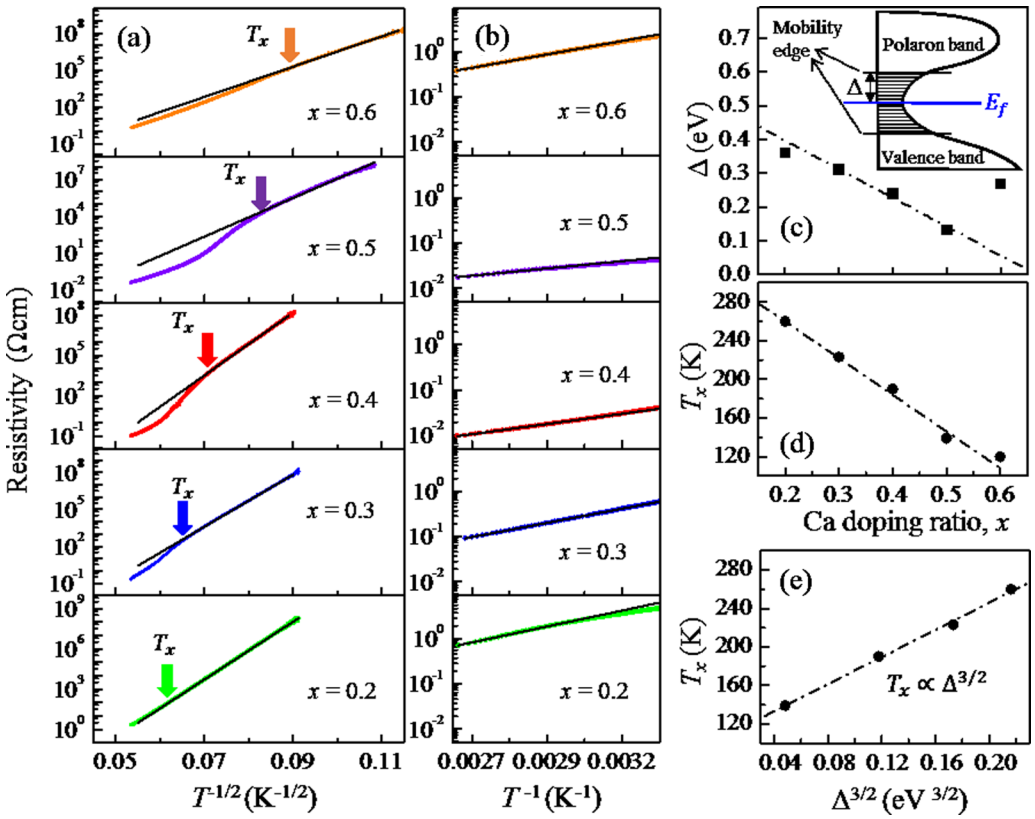

FIG. 3. Electronic conduction property of hole-doped BCFO films. (a) Logarithmic resistivity versus temperature to the power of $-1/2$. Each resistivity curve can be fitted to a linear curve (black line) at low temperatures, suggesting the ES-VRH behavior. In addition, thermal excitation to the delocalized band above the mobility edge can offer another route for electronic transport at high temperatures. (b) Logarithmic resistivity versus inverse temperature in the high-temperature regime. The linear fit curve (black line) gives the Arrhenius-type activation energy. (c) The activation energy for the thermal excitation versus x. (Inset) Schematic for the band structure with a soft gap. The shaded area represents localized states due to disorder. (d) Crossover temperature versus x. (e) Correlation between T_x and Δ.

mobility edge to an empty state above the Fermi level (holelike particle) or thermal excitation from the Fermi level to an empty state above the upper mobility edge (quasielectronic polaron) is necessary in order to create delocalized carriers. The resistance follows the typical semiconducting transport, i.e., $\rho = \rho_0 \exp(\Delta/k_B T)$, where Δ is a thermal activation energy and k_B is the Boltzmann constant. Below T_x, this thermal excitation is nearly suppressed and instead carrier hopping via tunneling among Coulomb-interacting localized states is dominant. In this low-temperature ES-VRH regime, electronic resistance can be written as $\rho = \rho_E \exp[(ce^2/\varepsilon\xi k_B T)^{1/2}]$, where c is a constant of order unity, ε is the dielectric constant, and ξ is the localization length [37].

Figure 3(c) summarizes the measured values of Δ extracted from the high-temperature data. As x increased, the activation energy linearly decreased with a minimum value of ∼120 meV observed at $x = 0.5$. This trend deviated at $x = 0.6$, which is a signature of another phase for $x > 0.5$. It has been reported that a charge-ordering phase emerges above $x = 0.5$ in $La_{1-x}Sr_xFeO_3$ [38,39]. It is also interesting that T_x systematically decreased with increase of hole concentration as well as Ca substitution [Fig. 3(d)]. The relation between Δ and T_x can be deduced from the fact that the two resistance equations give a similar value at T_x. Supposing the prefactors ρ_0 and ρ_E are of similar order of magnitude, the exponents of the two equations should be nearly equal and hence T_x is linearly proportional to $\xi\Delta^2$. Because the localization length ξ can be expressed as $3\hbar/\sqrt{8m\Delta}$, where m is the effective electronic mass and $\hbar$ is Planck's constant divided by 2π [40], T_x is linearly proportional to $\Delta^{3/2}$, as experimentally confirmed in Fig. 3(e). It is worthwhile mentioning that Masó and West found that the bulk sample processed in a high oxygen pressure displayed a perfect activated behavior above 200 K with an activation energy of 0.4 eV at $x = 0.3$ [27]. This discrepancy with our case of $T_x \sim 220$ K at $x = 0.3$ is due to the fact that the oxygen-vacancy reduction through the annealing in high oxygen pressure is an order of magnitude smaller than in our electrical formation process. The annealed bulk sample provides a quite different situation in terms of an order-of-magnitude larger oxygen-vacancy concentration but an order-of-magnitude smaller hole concentration regardless of having the same Ca content.

IV. EMERGENCE OF A NONRIGID BAND IN THE HOLE-DOPED REGIONS

To further clarify the electronic structure, we carried out two independent spectroscopic measurements, i.e., XPS to probe the valence band and the PEEM-based x-ray absorption spectroscopy at the oxygen K edge to investigate the

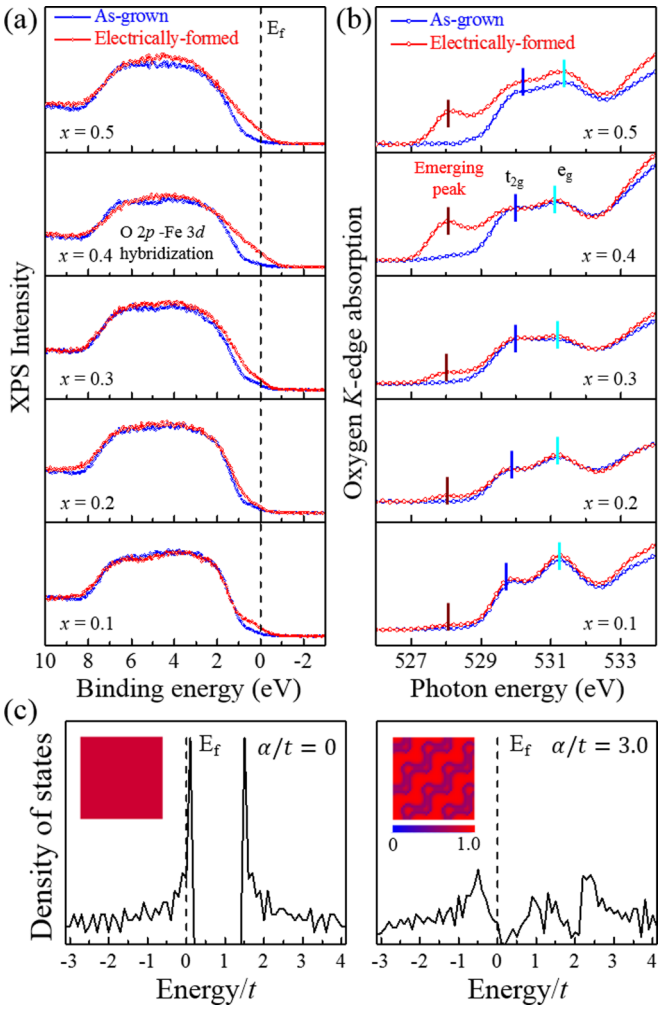

FIG. 4. Changes in the electronic structure of BCFO films. (a) Valence band structure investigated by XPS. (b) Oxygen K-edge x-ray absorption spectra acquired by PEEM. Subpeaks at 528 eV are recognized in the spectra obtained in the electrically formed areas. (c) The Hartree-Fock calculation results for the two-dimensional Holstein-Hubbard model in the adiabatic limit with different electron-lattice coupling strengths. (Insets) Charge density maps for 40×40 lattices. A phase separation occurs in the case of a large electron-lattice coupling, creating a soft gap near the Fermi level.

conduction band [Figs. 4(a) and 4(b); see Appendices C for the experimental details]. The conduction bands of as-grown samples have two peaks because the fivefold-degenerate Fe $3d$ level splits into two levels (t_{2g} and e_g) due to the ligand field of the oxygen octahedron. Regardless of a significant change in calcium content, the conduction band exhibits a similar feature of vacant $3d^6$ orbitals because of the same valence state of Fe^{3+}. In the spectra for the electrically formed regions, a new peak at ~528 eV below the t_{2g} level with a broadness of ~1 eV emerges, and the peak intensity consistently increases with x. Considering that our as-grown films are partially transparent in the visible range, similarly to a pure BFO film, their optical gaps are expected to be larger than 2.5 eV [16]. Thus, the peak emerging in the mid-gap cannot be understood by simple one-electron band filling. If the vacant upper part of the *rigid* valence band ascribed to hole doping were the origin, the peak would be expected at a lower energy by the band gap.

The emergence of the nonrigid band is most likely due to a strong electron-lattice coupling effect [41,42]. It is known that strong electron-phonon interaction can induce low-frequency phonons and small polarons with a large effective mass, creating a soft gap [43,44]. We note that similar nonrigid bands have been observed in other transition metal oxides such as $La_{1-x}Sr_xFeO_3$ and $La_{2-x}Sr_xCuO_4$ and their physical origins have been discussed in the context of the polaronic model [45–47] and the Zhang-Rice singlet [48], respectively. Our Hartree-Fock calculations of the Holstein-Hubbard model in the adiabatic limit (see Appendix D) also showed a similar gap formation in the density of states near the Fermi level alongside a spatial inhomogeneity in charge density at a strong electron-lattice coupling constant [Fig. 4(c)]. We would like to emphasize that the nanoscale spatial inhomogeneity is an intrinsic property similar to the phase separation of the colossal-magnetoresistance materials, where two insulating and metallic states are competing [49]. The split of the major XPS peak, the decrease of the structural correlation length, and its reversible recovery by thermal annealing in air at 250 °C (not shown here), as well as the emergence of the nonrigid polaronic band consistently indicate the occurrence of intrinsic phase separation in this system. This model Hamiltonian calculation is also in accordance with the experimental observations in terms of the fact that the strong electron-lattice coupling induces Coulomb attraction among carriers, leading to condensation of charge carriers, i.e., intrinsic phase separation. Hole-rich regions experience a more negative potential because of lattice deformation to screen the charge, and hence the emerging hole band is placed at a shifted position close to the conduction band minimum, creating a charge gap.

Despite the successful explanation of the electronic band structure, the sole consideration of electron-lattice and electron-electron interactions is not enough to explain the Coulomb-glass behavior yet. It is necessary to additionally introduce disorder associated with residual oxygen vacancies that can be controlled by electrical formation. Disorder causes irregular distributions of high- and low-hole-density regions. The states near the charge gap are thus localized and pinned spatially near the boundaries between the hole-rich and -poor regions, while electronic states far inside hole-rich regions produce a delocalized band corresponding to the emerging peak. The localized carriers interact with each other via a long-range Coulomb interaction and can hop to neighboring sites according to the ES-VRH mechanism. The localized states can also be thermally excited from the Fermi level to above the mobility edge of the polaronic band by gaining an energy of Δ and become itinerant in a delocalized state inside the charge cloud. In addition to the intrinsic phase separation and conduction mechanism, the possible engagement of a nonuniform defect distribution such as filamentary conduction paths is an important remaining topic to explore.

In addition, the valence band at binding energies ranging from 1 to 7 eV originates from oxygen $2p$ orbitals hybridized with Fe $3d$ orbitals. We note that the entire spectral weight of the valence band does not change significantly regardless of considerable Ca substitution. This seemingly contradictory

result is due to the fact that the electrical formation induces a topotactic transition, in which the numbers of constituent elements are not conserved [50,51]. Although hole doping is expected to reduce the spectral weight of the valence band, the addition of oxygen ions accompanied by an increase of oxygen $2p$ levels compensates the reducing effect and instead the added spectral weight contributes to the emerging band. These comprehensive studies on the electrically formed conducting areas and the systematic comparisons with the as-grown areas provide useful insights into microscopic electronic behaviors of defect-controlled oxides.

V. CONCLUSIONS

In summary, the electrical formation turned out to remove oxygen vacancies at elevated temperatures, thereby generating significant spectral weight primarily controlled by calcium content above the chemical potential. In the heavy-hole-doped BFO with both calcium acceptors and oxygen-vacancy donors, we found a Coulomb-glass transport phenomenon where two major conduction mechanisms via thermal excitation or tunneling among localized Coulomb-interacting states are competing, leading to a crossover behavior in the temperature-dependent resistance curves. The ES-VRH hopping mechanism is dominant in the lower-temperature regime, satisfying a scaling relation where T_x is linearly proportional to $\Delta^{3/2}$. The emergent polaronic band involved with intrinsic inhomogeneous charge distributions alongside the disorder inevitable for defect-containing materials is responsible for this Coulomb-glass phenomenon, originating from strong electron-lattice coupling effects and the phonon instability inherent in a quantum paraelectric driven by calcium substitution into a ferroelectric state. Thermal hopping into the polaronic band is a unique feature distinct from the semiconductor-based Coulomb glasses. These findings deepen our understanding of electronic behavior in hole-doped BFO and the microscopic interplay of oxygen vacancies and electronic conduction. Furthermore, the introduction of an additional technique to control oxygen content in insulating oxides can contribute to future studies of functional defects.

ACKNOWLEDGMENTS

This work was supported by a National Research Foundation (NRF) of Korea Grant funded by the Korean Government (Contracts No. NRF-2014R1A2A2A01005979, No. 2016R1A5A1008184, and No. NRF-2013S1A2A2035418) and by the Global Frontier Hybrid Interface Materials of the NRF of Korea funded by the Korea Government (Grant No. 2013M3A6B1078872). K.S. was also supported by the Ministry of Education, Science, and Technology (Grants No. NRF-2015R1C1A1A01051629 and No. 2011-0030785) of the NRF of Korea. J.S. acknowledges funding from the Australian Research Council. PEEM measurements were performed at the beamline BL25SU, SPring-8, with the approval of the Japan Synchrotron Radiation Research Institute under Proposals No. 2013A1028 and No. 2013B1079.

APPENDIX A: SAMPLE GROWTH AND X-RAY DIFFRACTION

BCFO thin films with various Ca substitution ratios (x = 0.1, 0.2, 0.3, 0.4, 0.5, and 0.6) were grown on (001) $SrTiO_3$ substrates using pulsed laser deposition. A KrF excimer laser ($\lambda = 248$ nm) was used to generate a laser fluence of $\sim$1 J/cm^2 at a repetition rate of 10 Hz. Growth temperatures were in the range of 650 to 700 °C and oxygen pressure for growths was adjusted to be 50 mTorr. BCFO films were grown to have approximately 100 nm in thickness. A 2-nm-thick $LaAlO_3$ film as a capping layer was deposited *in situ* right after the BCFO growth for the purpose of preventing oxygen reaction with the atmosphere during electrical formation. These films were cooled down to room temperature at a rate of 10 °C/min in an oxygen environment of 500 Torr. The crystal structures of BCFO thin films were examined by using an x-ray diffractometer (PANalytical X'pert MRD Pro) with Cu $K\alpha_1$ radiation. The Vegard lines interpolating between the c-axis lattice parameters of the two end compounds were calculated as the follow. For the as-grown compounds with the fixed valence state of Fe^{3+} ($\delta = x/2$), the c-axis lattice parameters of BFO and $CaFeO_{2.5}$ fully strained on a (001) $SrTiO_3$ substrate are 4.064 and 3.697 Å, respectively [5]. In addition, the case of stoichiometric compounds ($\delta = 0$) employs $CaFeO_3$ (for $x = 1$) which has an orthorhombic structure with $a = 5.350$ Å, $b = 7.536$ Å, and $c = 5.324$ Å [52] and thus the c-axis lattice parameter of a fully strained $CaFeO_3$ film on $SrTiO_3$ can be estimated to be 3.519 Å on the assumption of volume conservation.

APPENDIX B: DEVICE FABRICATION, ELECTRICAL FORMATION PROCESS, AND TRANSPORT MEASUREMENT

UV lithography was used to define electrode patterns on top of BCFO films and Pt electrodes were deposited by DC sputtering. *In situ* Ar ion milling was conducted to remove the capping layer right before all Pt depositions. An external formation voltage was applied between the coplanar electrodes at 250 °C to create nonequilibrium but long-lasting oxygen-vacancy-deficient states locally. The separation of the coplanar electrodes and the applied voltage were chosen differently depending on instrumental spatial resolutions. The *in situ* monitoring currents and PEEM spectra were obtained using pairs of electrodes with a separation of 20 μm to which a formation voltage of 15 V was applied for $\sim$1 h, while the electronic transport measurements were made at formation conditions of 100 μm, 20 V, and $\sim$1 h, and the x-ray diffraction and XPS used a wide gap of 1 mm along with formation at 25 V for $\sim$3 h. An abrupt increase of *in situ* monitoring current during each electrical formation process indicated the moment that a conducting path formed by showing a dark optical contrast between the electrodes. Another pair of Pt electrodes on the same film was prepared to define a reference region not exposed to electric voltage for comparison. For the electronic transport measurements, additional Pt electrodes (13 μm width and interval) were deposited *ex situ* after the electrical formation at the central formation region. The resistance was acquired by measuring the current at a bias of 10 V using

an electrometer (Keithley 6517B) with cooling temperature at a rate of -3 K/min inside a physical property measurement system (Quantum Design, Inc.). The resistivity curves at the high temperatures were obtained using the four-point-probe method by detecting voltage between 2-μm-distant electrodes at a constant current of 100 nA.

APPENDIX C: PHOTOEMISSION SPECTROSCOPIES

The oxygen stoichiometry and the valence band were examined by XPS. Photoelectrons were emitted by x rays (Al $K\alpha$, 1486.6 eV) incident at 54.7° to the sample surface with an in-plane projected direction along [100]. They were captured by an electron analyzer (K-alpha, Thermo Scientific). The regions concerned were etched *in situ* by Ar ion milling (EX06 Ion Source) to remove the capping layer and possible surface contaminants. All spectra were normalized by the integrated intensity of an Fe $2p$ peak obtained from the same area.

PEEM measurements were performed at beamline BL25SU of SPring-8 using circular polarized x rays incident at an angle of 30° to the sample surface with an in-plane projected direction along [100]. In order to remove charging effects during PEEM measurements, a thin Au layer ($\sim$2 nm thickness) was deposited on the exterior areas of the formed and unformed regions. The PEEM images were spatially uniform in the majority of interelectrode areas except for the narrow strip near the negatively biased electrode where oxygen vacancies piled up. The oxygen K-edge x-ray absorption spectra plotted in this paper were acquired at the central regions of the PEEM images, which exhibited spatially uniform signals. The spatial resolution of the PEEM was 100 nm. All x-ray absorption spectra were normalized by the counts measured at neighboring Pt electrodes.

APPENDIX D: MODEL HAMILTONIAN CALCULATION

To theoretically explore the emergence of the polaronic band based on the electron-lattice interaction, we employed the Holstein-Hubbard Hamiltonian [44]

$$H = \sum_{\langle i,j\rangle\sigma} t_{ij}\, c_{i\sigma}^{\dagger} c_{j\sigma} + U \sum_{i} n_{i\uparrow} n_{i\downarrow} - \sum_{i\sigma} g c_{i\sigma}^{\dagger} c_{i\sigma} (b_i^{\dagger} + b_i) + \sum_{i} \omega_0 b_i^{\dagger} b_i . \quad \text{(D1)}$$

Here, t_{ij} and U are the hopping integral and the on-site Coulomb repulsion energy, respectively. $\langle i,j\rangle$ stands for summation only over the nearest neighbors. $c_{i\sigma}^{\dagger}$ ($c_{j\sigma}$) is the creation (annihilation) operator for an electron with spin σ at lattice site i and $n_{i\sigma}$ is the corresponding number operator. In addition, $b_i^{\dagger}$ (b_i) is the phonon creation (annihilation) operator, ω_0 is a phonon frequency, and g is the electron-lattice interaction strength. In the adiabatic limit, the last phonon energy can be replaced by the static lattice deformation energy, i.e., $\sum_i \frac{1}{2} M {\omega_0}^2 {X_i}^2$, where X_i is the ionic coordinate operator equal to $(1/\sqrt{2M\omega_0})(b_i^{\dagger} + b_i)$ and M is the ionic mass. Accordingly, the Hamiltonian can be rewritten as

$$H = \sum_{\langle i,j\rangle\sigma} t_{ij}\, c_{i\sigma}^{\dagger} c_{j\sigma} + U \sum_{i} n_{i\uparrow} n_{i\downarrow} - \sum_{i\sigma} \tilde{g} n_{i\sigma} X_i + \sum_{i} \frac{1}{2} M {\omega_0}^2 {X_i}^2 . \quad \text{(D2)}$$

The electron-lattice coupling strength was renormalized as $\tilde{g} = \sqrt{2M\omega_0} g$. Since the intercoupling term can be expanded by mean-field approximation as

$$n_{i\sigma} X_i \cong n_{i\sigma} \langle X_i \rangle + \langle n_{i\sigma} \rangle X_i - \langle n_{i\sigma} \rangle \langle X_i \rangle , \quad \text{(D3)}$$

the Hamiltonian under the Hartree-Fock approximation becomes

$$\begin{aligned} H &= H_{\mathrm{el}} + H_{\mathrm{el-lattice}} + H_{\mathrm{lattice}}, \\ H_{\mathrm{el}} &\cong \sum_{\langle i,j\rangle\sigma} t_{ij}\, c_{i\sigma}^{\dagger} c_{j\sigma} + U \sum_{i\sigma} \left(\frac{1}{2} \langle n_i \rangle - \sigma \left\langle S_i^z \right\rangle \right) c_{i\sigma}^{\dagger} c_{i\sigma} \\ &\quad + U \sum_{i} \left[\left\langle S_i^z \right\rangle^2 - \frac{1}{4} \langle n_i \rangle^2 \right], \\ H_{\mathrm{el-lattice}} &\cong -\tilde{g} \sum_{i,\sigma} \langle X_i \rangle c_{i\sigma}^{\dagger} c_{i\sigma}, \\ H_{\mathrm{lattice}} &\cong \sum_{i} \frac{1}{2} M {\omega_0}^2 {X_i}^2 - \tilde{g} \sum_{i} \langle n_i \rangle X_i + \tilde{g} \sum_{i} \langle n_i \rangle \langle X_i \rangle , \end{aligned} \quad \text{(D4)}$$

where the expectation values of electron and spin densities were defined to be $\langle n_i \rangle = \langle n_{i\uparrow} \rangle + \langle n_{i\downarrow} \rangle$ and $\langle S_i^z \rangle = \frac{1}{2} (\langle n_{i\uparrow} \rangle - \langle n_{i\downarrow} \rangle)$. Given an electron density, the lattice energy can be minimized when the lattice is subject to the static deformation of $X_i = \tilde{g} \langle n_i \rangle / M\omega_0^2$. Finally, the Holstein-Hubbard Hamiltonian in the adiabatic limit can be reduced to the following solvable one-electron Hamiltonian :

$$\begin{aligned} H &\cong \sum_{\langle i,j\rangle\sigma} t_{ij}\, c_{i\sigma}^{\dagger} c_{j\sigma} + U \sum_{i\sigma} \left(\frac{1}{2} \langle n_i \rangle - \sigma \left\langle S_i^z \right\rangle \right) c_{i\sigma}^{\dagger} c_{i\sigma} \\ &\quad + U \sum_{i} \left[\left\langle S_i^z \right\rangle^2 - \frac{1}{4} \langle n_i \rangle^2 \right] - \alpha \sum_{i,\sigma} \langle n_i \rangle c_{i\sigma}^{\dagger} c_{i\sigma} \\ &\quad + \frac{\alpha}{2} \sum_{i} \langle n_i \rangle^2 , \end{aligned} \quad \text{(D5)}$$

where α is the electron-lattice coupling constant defined as $2g^2/\omega_0$.

The calculations for the model Hamiltonian for a two-dimensional square lattice (40×40) were performed to clarify the role of the electron-lattice interaction, which is expected to be significant because the parent BFO compound is ferroelectric and has strong electron correlation. The calculations were made at $U/t = 4.0$ and $k_B T = 0.2t$ with an average electron density of 0.8 per site and varying the electron-lattice coupling constant α. A periodic boundary condition was used and the convergence tolerance was 10^{-7}. Despite the simplified model, it did reflect the essential features of the BCFO. For zero α, we got a homogeneous electron density and a metallic state without any gap at the Fermi level at such high hole density. On the other hand, turning on the electron-lattice coupling gave

rise to a charge-density-wave instability. The electron density was inhomogeneous with a gap opening at the Fermi level. The part of the lower Hubbard band above the Fermi level was greatly shifted close to the upper Hubbard band, which shows a good agreement with the observations in the electronic structure of BCFO films. The real BCFO system additionally has high randomness arising from the dopant distribution, which most likely produces irregular polaron clouds. Since the localized state near the phase boundaries in real space corresponds to the one-electron state near the Fermi level, the hopping among the localized states along the phase boundaries is thought to be the main route for electronic conduction. We note that the (001) x-ray diffraction peaks detected in the electrically formed regions were broader than those of the as-grown states. This fact can be also related to the phase separation.

It is worth mentioning that the t_{2g} orbitals, i.e., d_{xy}, d_{yz}, and d_{zx}, consisting of the conduction band, are orthogonal to each other and thus on-site interorbital d-d hopping is not allowed. Moreover, intersite hopping is also prohibited between different types of orbitals at nearest-neighboring sites because as-grown BCFO films are tetragonal and no significant Fe-O-Fe buckling is expected [5]. Only orbitals of the same type can be hybridized with each other via oxygen π bonding within the specific two-dimensional plane where the relevant $3d$ and oxygen $2p$ orbitals are most probable (e.g., an electron in a d_{xy} orbital can hop along the x or y axis to a neighboring d_{xy} orbital within the xy-plane square lattice containing the orbital). Accordingly, the two-dimensional Hamiltonian can be a good starting model for understanding the BCFO system in the limit of small on-site effective U, but the dimensionality issue still remains unexplored.

[1] J. Jeong, N. Aetukuri, T. Graf, T. D. Schladt, M. G. Samant, and S. S. P. Parkin, Suppression of metal-insulator transition in VO_2 by electric field–induced oxygen vacancy formation, Science **339**, 1402 (2013).

[2] R. J. Cava, B. Batlogg, C. H. Chen, E. A. Rietman, S. M. Zahurak, and D. Werder, Oxygen stoichiometry, superconductivity and normal-state properties of $YBa_2Cu_3O_{7-\delta}$, Nature (London) **329**, 423 (1987).

[3] C. Ritter, M. R. Ibarra, J. M. De Teresa, P. A. Algarabel, C. Marquina, J. Blasco, J. García, S. Oseroff, and S.-W. Cheong, Influence of oxygen content on the structural, magnetotransport, and magnetic properties of $LaMnO_{3+\delta}$, Phys. Rev. B **56**, 8902 (1997).

[4] J. S. Lee, S. Lee, and T. W. Noh, Resistive switching phenomena: A review of statistical physics approaches, Appl. Phys. Rev. **2**, 031303 (2015).

[5] C.-H. Yang *et al.*, Electrical modulation of conduction in multiferroic Ca-doped $BiFeO_3$ films, Nat. Mater. **8**, 485 (2009).

[6] J. J. Yang, M. D. Pickett, X. Li, D. A. A. Ohlberg, D. R. Stewart, and R. S. Williams, Memristive switching mechanism for metal/oxide/metal nanodevices, Nat. Nanotechnol. **3**, 429 (2008).

[7] H. Jeen *et al.*, Reversible redox reactions in an epitaxially stabilized $SrCoO_x$ oxygen sponge, Nat. Mater. **12**, 1057 (2013).

[8] A. Kumar, F. Ciucci, A. N. Morozovska, S. V. Kalinin, and S. Jesse, Measuring oxygen reduction/evolution reactions on the nanoscale, Nat. Chem. **3**, 707 (2011).

[9] D. Lee, S. H. Baek, T. H. Kim, J.-G. Yoon, C. M. Folkman, C. B. Eom, and T. W. Noh, Polarity control of carrier injection at ferroelectric/metal interfaces for electrically switchable diode and photovoltaic effects, Phys. Rev. B **84**, 125305 (2011).

[10] C.-H. Yang, D. Kan, I. Takeuchi, V. Nagarajan, and J. Seidel, Doping $BiFeO_3$: Approaches and enhanced functionality, Phys. Chem. Chem. Phys. **14**, 15953 (2012).

[11] D. N. Mueller, M. L. Machala, H. Bluhm, and W. C. Chueh, Redox activity of surface oxygen anions in oxygen-deficient perovskite oxides during electrochemical reactions, Nat. Commun. **6**, 6097 (2015).

[12] P. Ágoston, P. Erhart, A. Klein, and K. Albe, Geometry, electronic structure and thermodynamic stability of intrinsic point defects in indium oxide, J. Phys.: Condens. Matter **21**, 455801 (2009).

[13] J. Seidel, P. Maksymovych, Y. Batra, A. Katan, S.-Y. Yang, Q. He, A. P. Baddorf, S. V. Kalinin, C.-H. Yang, J.-C. Yang, Y.-H. Chu, E. K. H. Salje, H. Wormeester, M. Salmeron, and R. Ramesh, Domain Wall Conductivity in La-Doped $BiFeO_3$, Phys. Rev. Lett. **105**, 197603 (2010).

[14] P. A. Lee and T. V. Ramakrishnan, Disordered electronic systems, Rev. Mod. Phys. **57**, 287 (1985).

[15] A. Biswas, K. S. Kim, and Y. H. Jeong, Metal insulator transitions in perovskite $SrIrO_3$ thin films, J. Appl. Phys. **116**, 213704 (2014).

[16] J. Seidel *et al.*, Prominent electrochromism through vacancy-order melting in a complex oxide, Nat. Commun. **3**, 799 (2012).

[17] H. Jang, G. Kerr, J. S. Lim, C.-H. Yang, C.-C. Kao, and J.-S. Lee, Orbital reconstruction in a self-assembled oxygen vacancy nanostructure, Sci. Rep. **5**, 12402 (2015).

[18] A. Ikeda-Ohno, J. S. Lim, T. Ohkochi, C.-H. Yang, and J. Seidel, Investigation of continuous changes in the electric-field-induced electronic state in $Bi_{1-x}Ca_xFeO_{3-\delta}$, Phys. Chem. Chem. Phys. **16**, 17412 (2014).

[19] K. K. Bharathi, W.-M. Lee, J. H. Sung, J. S. Lim, S. J. Kim, K. Chu, J. W. Park, J. H. Song, M.-H. Jo, and C.-H. Yang, Detection of electrically formed photosensitive area in Ca-doped $BiFeO_3$ thin films, Appl. Phys. Lett. **102**, 012908 (2013).

[20] C. Ederer and N. A. Spaldin, Weak ferromagnetism and magnetoelectric coupling in bismuth ferrite, Phys. Rev. B **71**, 060401(R) (2005).

[21] L. W. Martin, S. P. Crane, Y.-H. Chu, M. B. Holcomb, M. Gajek, M. Huijben, C.-H. Yang, N. Balke, and R. Ramesh, Multiferroics and magnetoelectronics: Thin films and nanostructures, J. Phys.: Condens. Matter **20**, 434220 (2008).

[22] G. Catalan, J. Seidel, R. Ramesh, and J. F. Scott, Domain wall nanoelectronics, Rev. Mod. Phys. **84**, 119 (2012).

[23] K. Chu *et al.*, Enhancement of the anisotropic photocurrent in ferroelectric oxides by strain gradients, Nat. Nanotechnol. **10**, 972 (2015).

[24] A. L. Efros and B. I. Shklovskii, *Electronic Properties of Doped Semiconductors* (Springer-Verlag, New York, 1984), Chap. 10.

[25] Y. M. Kim, J. He. M. D. Biegalski, H. Ambaye, V. Lauter, H. M. Christen, S. T. Pantelides, S. J. Pennycook, S. V. Kalinin, and A. Y. Borisevich, Proving oxygen vacancy concentration and homogeneity in solid-oxide fuel-cell cathode materials on the subunit-cell level, Nat. Mater. **11**, 888 (2012).

[26] H. Ullmann and N. Trofimenko, Estimation of effective ionic radii in highly defective perovskite-type oxides from experimental data, J. Alloys Compd. **316**, 153 (2001).

[27] N. Masó and A. R. West, Electrical properties of Ca-doped $BiFeO_3$ ceramics: From p-type semiconduction to oxide-ion conduction, Chem. Mater. **24**, 2127 (2012).

[28] D. Reznik, L. Pintschovius, M. Ito, S. Iikubo, M. Sato, H. Goka, M. Fujita, K. Yamada, G. D. Gu, and J. M. Tranquada, Electron-phonon coupling reflecting dynamic charge inhomogeneity in copper oxide superconductors, Nature (London) **440**, 1170 (2006).

[29] J. X. Ma, D. T. Gillaspie, E. W. Plummer, and J. Shen, Visualization of Localized Holes in Manganite Thin Films with Atomic Resolution, Phys. Rev. Lett. **95**, 237210 (2005).

[30] M. Capone, G. Sangiovanni, C. Castellani, C. D. Castro, and M. Grilli, Phase Separation Close to the Density-Driven Mott Transition in the Hubbard-Holstein Model, Phys. Rev. Lett. **92**, 106401 (2004).

[31] J. W. Lynn, D. N. Argyriou, Y. Ren, Y. Chen, Y. M. Mukovskii, and D. A. Shulyatev, Order and dynamics of intrinsic nanoscale inhomogeneities in manganites, Phys. Rev. B **76**, 014437 (2007).

[32] B. D. Cullity and S. R. Stock, *Elements of X-ray Diffraction*, 3rd ed. (Prentice-Hall, Englewood Cliffs, NJ, 2001), p. 170.

[33] D. Yu, C. Wang, B. L.Wehrenberg, and P. Guyot-Sionnest, Variable Range Hopping Conduction in Semiconductor Nanocrystal Solids, Phys. Rev. Lett. **92**, 216802 (2004).

[34] E. Helgren, N. P. Armitage, and G. Grüner, Electrodynamics of a Coulomb Glass in n-Type Silicon, Phys. Rev. Lett. **89**, 246601 (2002).

[35] A. M. Somoza, M. Ortuño, M. Caravaca, and M. Pollak, Effective Temperature in Relaxation of Coulomb Glasses, Phys. Rev. Lett. **101**, 056601 (2008).

[36] S. Pankov and V. Dobrosavljević, Nonlinear Screening Theory of the Coulomb Glass, Phys. Rev. Lett. **94**, 046402 (2005).

[37] A. L. Efros and B. I. Shklovskii, Coulomb gap and low temperature conductivity of disordered systems, J. Phys. C: Solid State Phys. **8**, L49 (1975).

[38] S. K. Park, T. Ishikawa, Y. Tokura, J. Q. Li, and Y. Matsui, Variation of charge-ordering transitions in $R_{1/3}Sr_{2/3}FeO_3$ (R = La, Pr, Nd, Sm, and Gd), Phys. Rev. B **60**, 10788 (1999).

[39] J. Blasco, B. Aznar, J. García, G. Subías, J. Herrero-Martín, and J. Stankiewicz, Charge disproportionation in $La_{1-x}Sr_xFeO_3$ probed by diffraction and spectroscopic experiments, Phys. Rev. B **77**, 054107 (2008).

[40] T. Chen and B. I. Shklovskii, Anomalously small resistivity and thermopower of strongly compensated semiconductors and topological insulator, Phys. Rev. B **87**, 165119 (2013).

[41] H. Wadati, D. Kobayashi, H. Kumigashira, K. Okazaki, T. Mizokawa, A. Fujimori, K. Horiba, M. Oshima, N. Hamada, M. Lippmaa, M. Kawasaki, and H. Koinuma, Hole-doping-induced changes in the electronic structure of $La_{1-x}Sr_xFeO_3$: Soft x-ray photoemission and absorption study of epitaxial thin films, Phys. Rev. B **71**, 035108 (2005).

[42] A. Chainani, M. Mathew, and D. D. Sarma, Electronic structure of $La_{1-x}Sr_xFeO_3$, Phys. Rev. B **48**, 14818 (1993).

[43] D. Meyer, A. C. Hewson, and R. Bulla, Gap Formation and Soft Phonon Mode in the Holstein Model, Phys. Rev. Lett. **89**, 196401 (2002).

[44] S. Ciuchi, F. de Pasquale, S. Fratini, and D. Feinberg, Dynamical mean-field theory of the small polaron, Phys. Rev. B **56**, 4494 (1997).

[45] W. H. Jung and E. Iguchi, Polaronic transport properties in $La_{1-x}Sr_xFeO_3$ systems ($0.05 < \text{or} = x < \text{or} = 0.3$), J. Phys.: Condens. Matter **7**, 1215 (1995).

[46] H. Wadati, A. Chikamatsu, M. Takizawa, R. Hashimoto, H. Kumigashira, T. Yoshida, T. Mizokawa, A. Fujimori, M. Oshima, M. Lippmaa, M. Kawasaki, and H. Koinuma, Strong localization of doped holes in $La_{1-x}Sr_xFeO_3$ from angle-resolved photoemission spectra, Phys. Rev. B **74**, 115114 (2006).

[47] A. Braun *et al.*, Electron hole–phonon interaction, correlation of structure, and conductivity in single crystal $La_{0.9}Sr_{0.1}FeO_{3-\delta}$, Appl. Phys. Lett. **93**, 262103 (2008).

[48] D. Meyers *et al.*, Zhang-Rice physics and anomalous copper states in A-site ordered perovskites, Sci. Rep. **3**, 1834 (2013).

[49] M. Uehara, S. Mori, C. H. Chen, and S. W. Cheong, Percolative phase separation underlies colossal magnetoresistance in mixed-valent mangatites, Nature (London) **399**, 560 (1999).

[50] Y. Tsujimoto, C. Tassel, N. Hayashi, T. Watanabe, H. Kageyama, K. Yoshimura, M. Takano, M. Ceretti, C. Ritter, and W. Paulus, Infinite-layer iron oxide with a square-planar coordination, Nature (London) **450**, 1062 (2007).

[51] H. Jeen, W. S. Choi, J. W. Freeland, H. Ohta, C. U. Jung, and H. N. Lee, Topotactic phase transformation of the brownmillerite $SrCoO_{2.5}$ to the perovskite $SrCoO_{3-\delta}$, Adv. Mater. **25**, 3651 (2013).

[52] T. Takeda *et al.*, Metal-semiconductor transition, charge disproportionation, and low-temperature structure of $Ca_{1-x}Sr_xFeO_3$ synthesized under high oxygen pressure, Solid State Sci. **2**, 673 (2000).